Visualizing the chemical incompatibility of halide and sulfide-based electrolytes in solid-state batteries

C. Rosenbach,[1] F. Walther,[2] J. Ruhl,[1] M. Hartmann,[1] T. A. Hendriks,[3] S. Ohno[4], J. Janek[2,*] and W. G. Zeier[1,3,*]

[1]*Institute of Inorganic and Analytical Chemistry, University of Münster (WWU), Corrensstrasse 28/30, 48149 Münster, Germany*

[2]*Institute of Physical Chemistry & Center for Materials Research (ZfM/LaMa), Justus Liebig University, Heinrich-Buff-Ring 17, 35392 Giessen, Germany*

[3]*Institut für Energie- und Klimaforschung (IEK), IEK-12: Helmholtz-Institut Münster, Forschungszentrum Jülich, Corrensstaße 46, Münster 48149, Germany*

[4]*Department of Applied Chemistry, Graduate School of Engineering, Kyushu University, 744 Motooka, Nishi-ku, 819-0395 Fukuoka, Japan*

**juergen.janek@phys.chemie.uni-muenster.de, wzeier@uni-muenster.de*

Abstract

Halide-based solid electrolytes are currently growing in interest in solid-state batteries due to their high electrochemical stability window compared to sulfide electrolytes. However, often a bilayer separator of a sulfide and a halide is used and it is unclear why such setup is necessary, besides the instability of the halides against lithium metal. We show that an electrolyte bilayer improves the capacity retention as it suppresses interfacial resistance growth monitored by impedance spectroscopy. By using in-depth analytical characterization of buried interphases by time-of-flight secondary ion mass spectrometry and focused ion beam scanning electron microscopy analyses, we detect an indium-sulfide rich region at the halide and sulfide contact area, visualizing the chemical incompatibility of these two electrolytes. The results highlight the need to consider more than just the electrochemical stability of electrolyte materials, showing that chemical compatibility of all components may be paramount when using halide-based solid electrolytes in solid-state batteries.

1. Introduction

Due to the increasing energy consumption and need for energy storage, lithium-ion batteries have become the most used battery technology for commercial applications. This widely used cell concept with a liquid electrolyte is close to the limits of its energy density which and a certain degree of safety concerns due to the flammability of organic solvents.[1] These disadvantages may be overcome using solid-state batteries.[1–3] By using inorganic solid electrolytes that exhibit high ionic conductivities in the $mS \cdot cm^{-1}$ range, organic solvents may be replaced.[4–6] A solid electrolyte class that fulfils the requirement of high ionic conductivity are sulfide-based materials of argyrodite type such as Li_6PS_5X (X = Cl, Br, I),[7–9] Li_3PS_4[10,11] or $Li_{10}GeP_2S_{12}$.[12,13] Based on their high ionic conductivity, stability against In/LiIn anode and advantageous mechanical properties (e.g. malleability), these sulfides are prominently used as electrolytes in solid-state battery studies.[2,14–18] Unfortunately, these compounds have a narrow thermodynamic stability window, leading to limitations in the cathode due to decomposition reactions,[2,16,19] for example the electrolyte Li_6PS_5Cl with $LiNi_{0.6}Co_{0.2}Mn_{0.2}O_2$ lead to PO_x and SO_x.[19] A promising class of solid electrolytes are halide-based materials with increased stability against typical cathode active materials (CAM), rediscovered by Asano *et al.* in 2018 using mechanochemical syntheses.[20] These compounds exhibit a wide range of compositions of the formula Li_6MX_6 (M^{3+} = metal, X = Cl, Br, I),[21–24] for example Li_3InCl_6,[25,26] Li_3YCl_6[27,28] or $Li_2Sc_{2/3}Cl_4$,[29] and show reasonable ionic conductivity values of $mS \cdot cm^{-1}$ at room temperature.[21–30] Based on their wider thermodynamic stability window and with it their suggested higher electrochemical stability against CAMs, when compared to the sulfide materials, this material class might be more suitable for the use in solid-state batteries with high voltage CAMs.[30,31] Nevertheless, recent work shows that while the halides may show high electrochemical stability (stability against a certain oxidation potential),[32] chemical stability (stability of the different cell components against side reactions) is not necessarily given.[33–35] Li_3InCl_6 is suggested to have both a high electrochemical stability window[30] and reasonable conductivity of greater than 1 $mS \cdot cm^{-1}$.[25,26] However, Li_3InCl_6 is not stable against lithium metal and decomposes, inhibiting its use as separator in solid-state batteries.[36] First cell studies with Li_3InCl_6 only as catholyte, together with $LiNi_{0.8}Co_{0.1}Mn_{0.1}O_2$ or $LiCoO_2$ show decent capacity values.[25,26] Clearly, Li_3InCl_6 is an interesting candidate as catholyte, but an additional sulfide layer is often used to prevent the halide decomposition in direct contact to the lithium metal anode.[25] Recently, a bi-layer approach has been increasingly used for the construction of separators, with a sulfide-based material contacting the anode and a halide solid electrolyte contacting the halide-based cathode composite.[33,37–39] This bilayer approach seems to disagree

with the overall goal of creating thinner separator layers for practical use of solid-state batteries. It is also in stark contrast to simple processing on large scale. In addition, it was recently found that the incompatibility of Li_3InCl_6 and Li_6PS_5Cl in $LiNi_{0.6}Co_{0.2}Mn_{0.2}O_2$-based cells lead to decomposition products and higher interfacial resistance,[34,35] suggesting possible issues with this approach. Nevertheless, no direct analyses of any ongoing chemical and electrochemical processes have been established to explain the chemical processes occurring at the respective interfaces.

Inspired by the question of why a bilayer separator is often used and what happens when it is missing, in this work, we study the halide electrolyte Li_3InCl_6 in combination with the CAM $LiNi_{0.8}Co_{0.1}Mn_{0.1}O_2$ and the separator material Li_6PS_5Cl. By choosing different solid-state battery setups (see Figure 1), we aim to better understand the influence of this additional layer. Electrochemical impedance spectroscopy and long-term cycling suggest that without the additional halide electrolyte layer, decomposition reactions occur between the sulfide solid electrolyte and the halide-based cathode composite. Although chemical analyses of buried interfaces are typically challenging, here we were able to analyze the ongoing reaction at the separator | cathode composite interphase. With ToF-SIMS (time-of-flight secondary ion mass spectrometry), FIB-SEM (focused ion beam scanning electron microscopy) analyses and with XPS (X-ray photoelectron spectroscopy) analyses the existence of indium sulfide-based decomposition products is confirmed. Overall, this work serves to show that the use of halide catholytes in solid-state batteries may not be as straightforward as currently believed, and that some unwanted decomposition pathways still exist and need to be considered in the search for new halide electrolytes.

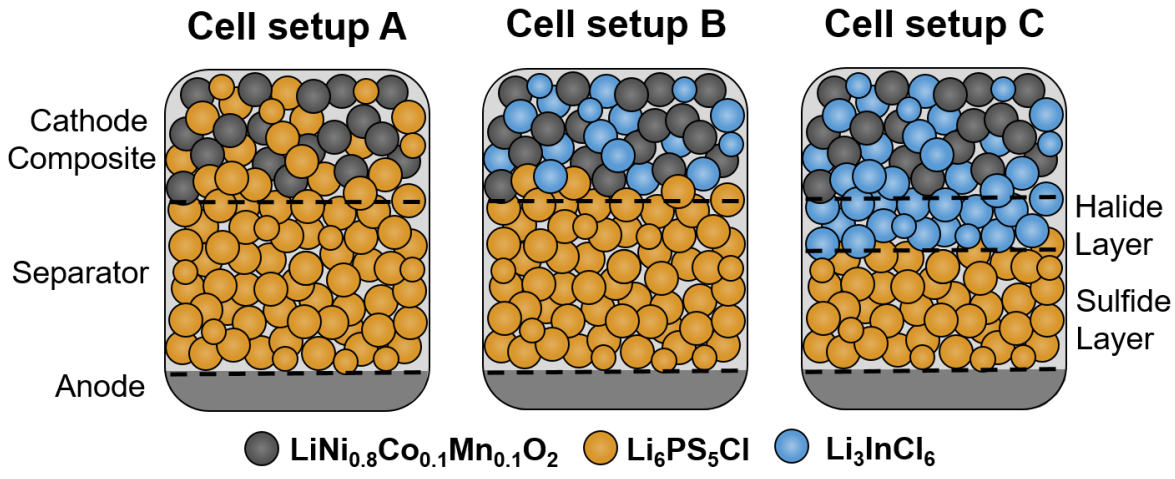

Figure 1: Scheme of the different cell setups with different separator and cathode composite combinations and $LiNi_{0.8}Co_{0.1}Mn_{0.1}O_2$ as CAM (black). Cell setup A with Li_6PS_5Cl (orange) as

the separator and catholyte: In/LiIn | Li_6PS_5Cl | Li_6PS_5Cl:$LiNi_{0.8}Co_{0.1}Mn_{0.1}O_2$. Cell setup B with Li_6PS_5Cl as separator and Li_3InCl_6 (blue) as catholyte: In/LiIn | Li_6PS_5Cl | Li_3InCl_6:$LiNi_{0.8}Co_{0.1}Mn_{0.1}O_2$. Cell setup C with Li_6PS_5Cl | Li_3InCl_6 as bilayer separator and Li_3InCl_6 as catholyte: In/LiIn | Li_6PS_5Cl | Li_3InCl_6 | Li_3InCl_6:$LiNi_{0.8}Co_{0.1}Mn_{0.1}O_2$.

2. Results

To reveal the reason for the typically used bilayer separator design and the underlying processes at the interfaces, in this study, the solid electrolytes Li_6PS_5Cl and Li_3InCl_6 were used as separator material and catholyte in different cell configurations. The following three different cell configurations are used and schematically shown in Figure 1:

Notation: anode | separator | composite cathode,
A) Cell setup A: In/LiIn | Li_6PS_5Cl | $LiNi_{0.8}Co_{0.1}Mn_{0.1}O_2$:$Li_6PS_5Cl$,
B) Cell setup B: In/LiIn | Li_6PS_5Cl | $LiNi_{0.8}Co_{0.1}Mn_{0.1}O_2$:$Li_3InCl_6$, and
C) Cell setup C: In/LiIn | Li_6PS_5Cl | Li_3InCl_6 | $LiNi_{0.8}Co_{0.1}Mn_{0.1}O_2$:$Li_3InCl_6$.

Both solid electrolytes were successfully synthesized and exhibited ionic conductivity values at 25 °C similar to those reported in the literature, namely $\sigma(Li_6PS_5Cl) = 1.3$ mS·cm^{-1}[7,15,40] and $\sigma(Li_3InCl_6) = 0.7$ mS·cm^{-1} [22,25,26]. The In/LiIn alloy is used as counter electrode to ensure a stable potential and no ongoing decomposition that would convolute the impedance analyses.[41] Detailed experimental information, refined X-ray diffractograms and the impedance spectra can be found in the Supporting Information and Figure S1-S2.

2.1 Cell cycling

All cell configurations were cycled between 2.0 V and 3.7 V *vs*. In/LiIn, corresponding to 2.6 V and 4.3 V *vs*. Li^+/Li, with a current density of 0.214 mA·cm^{-2}. Figures 2 a), b) and c) show the potential profiles for the charging and discharging steps of the three different cell setups. The pure sulfide-based cell (cell setup A, orange) shows the highest initial charge capacity of 217 mAh·g^{-1} (2.32 mAh·cm^{-2}), followed by the halide cell with Li_3InCl_6 in the cathode composite (cell setup B, green) with 200 mAh·g^{-1} (1.83 mAh·cm^{-2}) and the bilayer-based cell (cell setup C, blue) with 176 mAh·g^{-1} (1.61 mAh·cm^{-2}). The lower initial charge capacity for cell setup C is likely due to higher bulk resistance caused by the comparably thick bilayer separator (see next section). The initial discharge capacity for all cells is 163 mAh·g^{-1}, 175 mAh·g^{-1} and 154 mAh·g^{-1}, for cell setups A, B and C, respectively. The trend of the

discharge capacities and the Coulomb efficiencies are shown for 100 cycles in the Supporting Information Figure S3. The differences in initial charge and discharge capacities are common in solid-state batteries and mainly result from irreversible structural rearrangement, chemo-mechanical effects and loss of available lithium.[42–44] In addition, the cathode material is prone to react with the sulfides electrolyte forming oxides such as PO_x or SO_x in the case of Li_6PS_5Cl.[19] Potential chemical decomposition of the halides has also been reported,[33] especially with Zr-based compounds that are very oxyphilic and attack the active material. Overall, the three cell setups show a trend comparable in performance to literature. Accordingly, pure sulfide cells with high nickel content $LiNi_xCo_yMn_zO_2$ typically show high initial capacities of over 200 $mAh \cdot g^{-1}$.[45] In comparison, halide-based cells usually show lower initial capacity values. For example, a carbon-containing $LiNi_{0.6}Co_{0.2}Mn_{0.2}O_2$- and Li_3InCl_6-based composite cathode has shown an initial charge capacity of 166 $mAh \cdot g^{-1}$[34], whereas a $LiNi_{0.85}Co_{0.1}Mn_{0.05}O_2$- and Li_3InCl_6-based composite exhibited an initial charge capacity slightly under 200 $mAh \cdot g^{-1}$.[33] The general shape of the charge/discharge curves is similar for all setups and is characteristic for the CAM. For example, the plateau in the charge curve at around 3.6 V (*vs.* In/InLi) is typical for $LiNi_{0.8}Co_{0.1}Mn_{0.1}O_2$ showing the conversion from the hexagonal H2 phase to the other hexagonal H3 phase.[43]

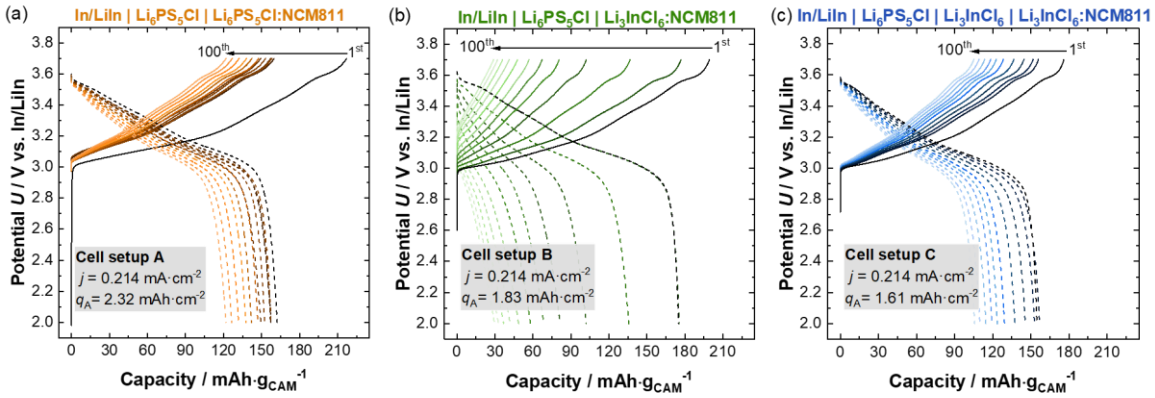

Figure 2: Charge and discharge curves of cell setups (a) A, (b) B and (c) C, cycled at 25 °C. The figures show the 1st, 2nd, 10th, 20th, 30th, 40th, 50th, 60th, 70th, 80th, 90th and 100th cycle of the cells colorized from darker to lighter color.

The overall capacity values from the first to the 100th cycle are shown for all cell setups in Figure 3. The charge capacity of cell setup A (orange) decreases from 217 $mAh \cdot g^{-1}$ to 122 $mAh \cdot g^{-1}$, showing an overall loss in capacity of 44 %. Cell setup B (green) shows the strongest capacity fading over cell cycling with an overall capacity loss of 86 % (200 $mAh \cdot g^{-1}$ to 29 $mAh \cdot g^{-1}$). By using the additional Li_3InCl_6 layer (cell setup C, blue) the capacity loss is

significantly reduced to 40 % (176 mAh·g^{-1} to 105 mAh·g^{-1}), highlighting the beneficial effect of the bilayer separator design. The more stable cell cycling behavior of cell setups A and C compared to cell setup B is also reflected in the Coulomb efficiencies (see Figure S3b). Accordingly, the Coulomb efficiencies of cell setup B scatter strongly, while they are more stable for the other two setups, indicating less detrimental side reactions in the latter cases. The more pronounced capacity fading upon cell cycling (Figure 3a) can be correlated to the average overpotential (Figure 3b). While extracting the average potential between 2.7 V and 3.7 V during charging as a function of the cycle number, cell setup B has the strongest increase compared to cell setup A and C.

Overall, based on the capacities and Coulomb efficiencies, the sulfide electrolyte-based cell shows the best performance. The beneficial effect of the bilayer separator design for halide-based composite cathodes is clearly evident from a reduced capacity fading and a slower overpotential evolution upon cell cycling.

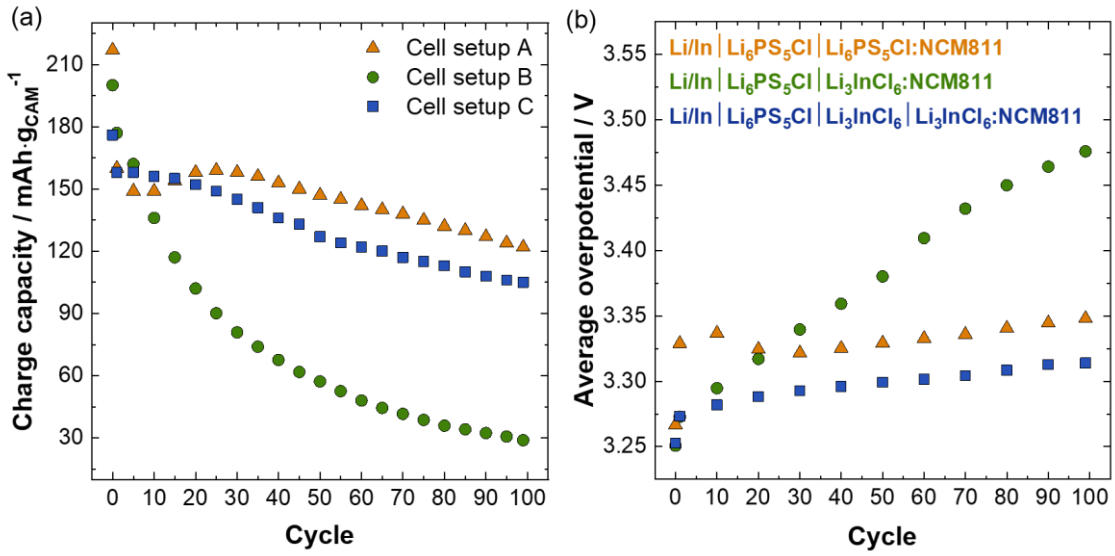

Figure 3: (a) Charge capacities and (b) average overpotential of the different cell setups, showing the most severe degradation when the halide catholyte is in direct contact to the sulfide separator.

2.2 Impedance analyses

To understand the underlying processes within the three different cell setups in more detail, impedance data were collected during cell cycling. Therefore, an impedance spectrum was

recorded after each charging and discharging step to quantify the different processes occurring at the interfaces in the cells as a function of time. The impedance data obtained after the 1st (b, d and f) and the 100th charging step (c, e and g) are shown in Nyquist plots in Figure 4 with their corresponding fits. A potentially insightful approach to extract transport parameters would be the use of transmission-line modeling of the impedance spectra, as has been performed quite successfully recently.[41,46–48] While transmission-line modeling in the here-investigated cells leads to comparable results for the first charge, the subsequent impedance spectra of the cycling process would require a change in the transmission-line model. At this stage changing fits cannot be corroborated without too many additional assumptions. Therefore, in order to monitor the impedance increase consistently, the data are analyzed with the equivalent circuit shown in Figure 4a, assuming four different transport/transfer processes based on previous literature.[15,16]

These four processes typically represent in the literature the resistance of the bulk of the electrolyte $R_{SE,bulk}$ (gray), a grain boundary-type resistance of the electrolyte $R_{SE,grain}$ (yellow), the resistance of the interface of the electrolyte and the CAM $R_{SE/CAM}$ (red) and the resistance of the interface of the electrolyte to the anode material $R_{SE/anode}$ (purple). The different processes were assigned based on the obtained capacitances of the different semicircles and the frequency range derived from previous impedance data analysis.[14–16,49] In addition, it remains unclear whether the mid-frequency signal really corresponds to the grain boundary contribution or whether it rather represents a geometric constriction effect in the catholyte.[50] At the lowest frequencies, a Warburg-type impedance behavior was observed, possibly related to lithium diffusion in the active materials.[14] Within this study the different extractable resistances where named R_1, R_2, R_3 and R_4 to avoid a direct relation to the physical process (see below). This is needed as the term $R_{SE/CAM}$ will not be directly the correct terminology to this interface process here (see later section). The fit results of the resistances, the capacitances, α-values (exponent of the constant phase element) as well as the frequency ranges of the assigned processes can be found in Table S1. The values obtained are in the range of previous works, indicating a strong overlap of relaxation times of the different processes.[14–16,49]

The first resistance R_1 in the high frequency range can be reliably assigned to $R_{separator}$ (gray) for all spectra and corresponds to a pre-resistance R in the equivalent circuit (Figure 4a). After the first charge, this resistance is comparably high for cell setup C, indicating that the additional halide layer (and thus thicker separator) causes to a higher total bulk resistance. In contrast, cell setup A and B show similar low values after the first charge. In the middle frequency range,

two resistances R_2 and R_3 are found. As discussed above, these are typically related to grain boundaries and the resistance at the CAM in the composite cathode, respectively. However, here we will, for the sake of simplicity $R_{\text{interface,1}}$ (yellow) and $R_{\text{interface,2}}$ (red) while keeping in mind that besides intrinsic interfaces, interphases may be growing. Both related processes are represented by a parallel resistor and constant-phase element (R/CPE) in the equivalent circuit (Figure 4a) and basically distinguished based on their different capacitances (see Tables S1-S3). However, due to low α-values and a strong overlap of time constants, the separation of the different processes is challenging, leading to wider error ranges. Clearly, assigning the processes correctly to the different relaxation times becomes difficult with the increasing number of interfaces and resulting interphases. Nevertheless, for a qualitative discussion these processes are disentangled with keeping in mind that the increase of one will affect the others. For all three cell setups, the value of $R_{\text{interface,1}}$ remains relatively stable after the first charge for all cell setups, whereas the values for $R_{\text{interface,2}}$ for cell setup A differ. A higher initial resistance is found for cell setup A that may be caused either by an irreversible chemical reaction of the sulfide electrolyte with the $LiNi_{0.8}Co_{0.1}Mn_{0.1}O_2$ particles,[16] or simply by a generally higher interfacial impedance. The low frequency processes R_4 can be correlated to $R_{\text{SE/anode}}$ (purple) and contribute the least to the total resistance in all spectra.

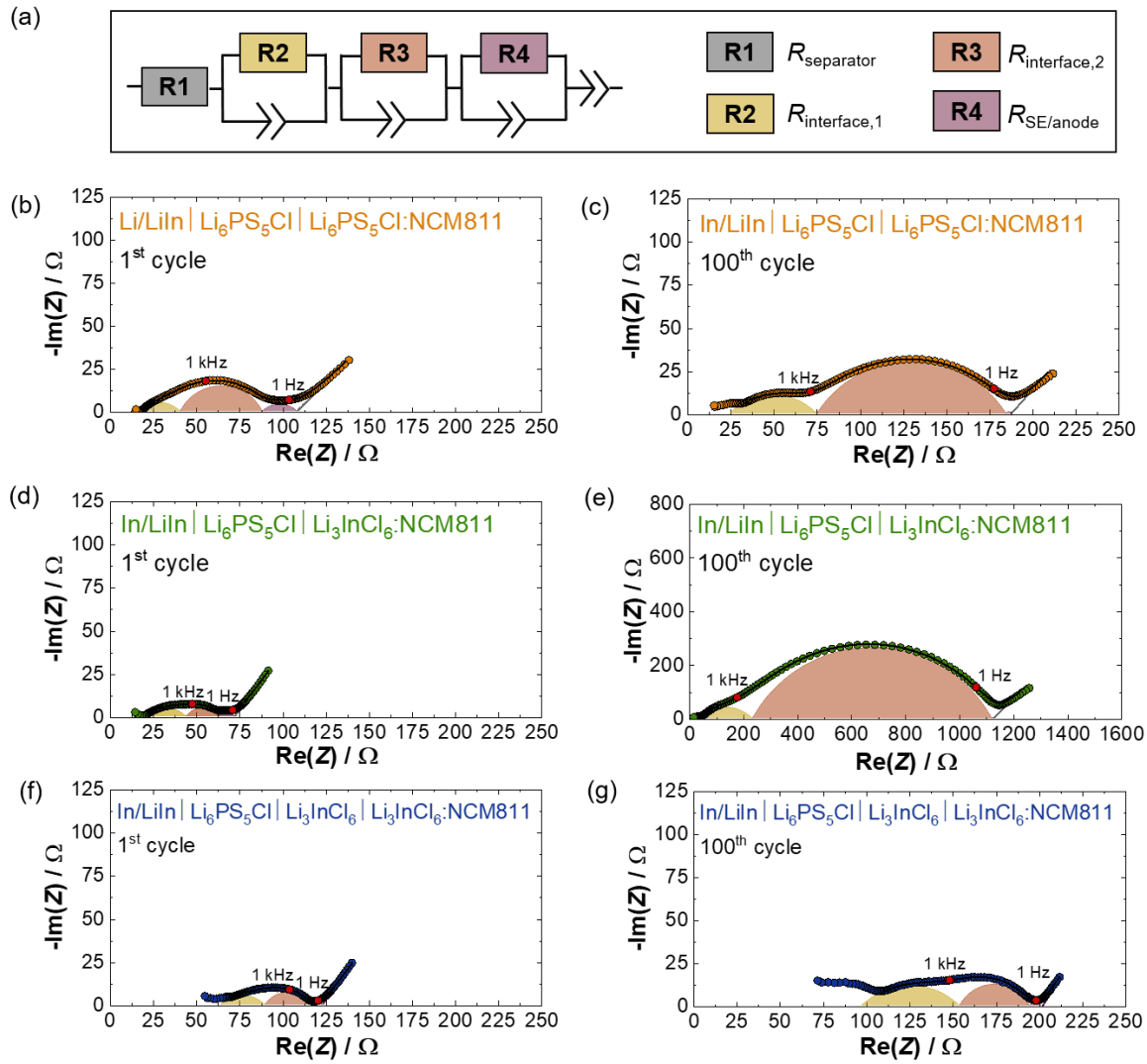

Figure 4: Nyquist plots of the impedance data (b-g) and the equivalent circuit used for fitting (a). Shown are spectra after the 1st and 100th cycle. (b) and (c) shows the impedance data for cell setup A (orange), (d) and (e) for cell setup B (green) and (f) and (g) for cell setup C (blue). Three microscopic transport/transfer steps are assigned to the semicircles: $R_{interface,1}$ (yellow), $R_{interface,2}$ (red) and $R_{SE/anode}$ (purple).

For a direct comparison of the three cell setups, the resistances obtained by fitting are shown as a function of the cycle number in Figure 5. R_1 starts at a similar value for cell setups A and B (orange and green) and shows a comparable increase upon cell cycling. In direct comparison, cell setup A exhibits a slightly reduced resistance due to the higher ionic conductivity of the separator. In contrast, cell setup C (blue) has an initially higher resistance (partially due to the thicker separator) but also shows a more pronounced increase upon cell cycling. This increase of the bilayer separator resistance has already been reported for Li_3InCl_6-based cells before.[33]

The high resistance and particularly the increase upon cell cycling appears to be caused by the recently reported chemical incompatibility between Li_3InCl_6 and Li_6PS_5Cl, which results in the formation of an interphase and thus to a higher resistance (see discussion section below).[34,35]

Considering the impedance evolution of R_2 and R_3 as a function of cycle number (Figure S 7 a, b), an increase over time was found in every cell type. At lower cycle numbers a deconvolution of both processes is challenging, at higher numbers the strongly increasing R_3 makes a deconvolution easier. Nevertheless, as it is difficult to rule out that the fitting of one R-CPE element influences the results of the other elements. Therefore, for a more indicative analysis, both resistances are shown as their sum (Figure 5b). Overall, the strongest changes are found for cell setup B. Increasing impedances are often caused by interfacial degradation reactions in solid-state batteries,[14,16,19] which bears the question which interface dominates the significant impedance evolution in the case of cell setup B. The assignment of the respective frequency range to an interface resistance $R_{interface,2}$ can imply that the degradation at the Li_3InCl_6 | $LiNi_{0.8}Co_{0.1}Mn_{0.1}O_2$ interface is causing the almost 50 times higher impedance.[51] However, the halide electrolyte | CAM interface is supposed to be electrochemically more stable compared to the sulfide-based counterpart.[30] In addition, if the halide electrolyte | CAM interface is responsible for the rise in impedance, similar observations should be observable for cell setup C. Indeed, the only difference between cell setup B and C is that of a triple phase boundary of $LiNi_{0.8}Co_{0.1}Mn_{0.1}O_2$, Li_6PS_5Cl and Li_3InCl_6, which is avoided in cell type C suggesting that strong decomposition reactions occur at the interface between the sulfide separator and the halide-based cathode composite. Clearly then, an additional layer of Li_3InCl_6 is needed, as it avoids the triple phase boundary and leads to more stability and suppresses fast capacity fading. This will be discussed in the further discussion.

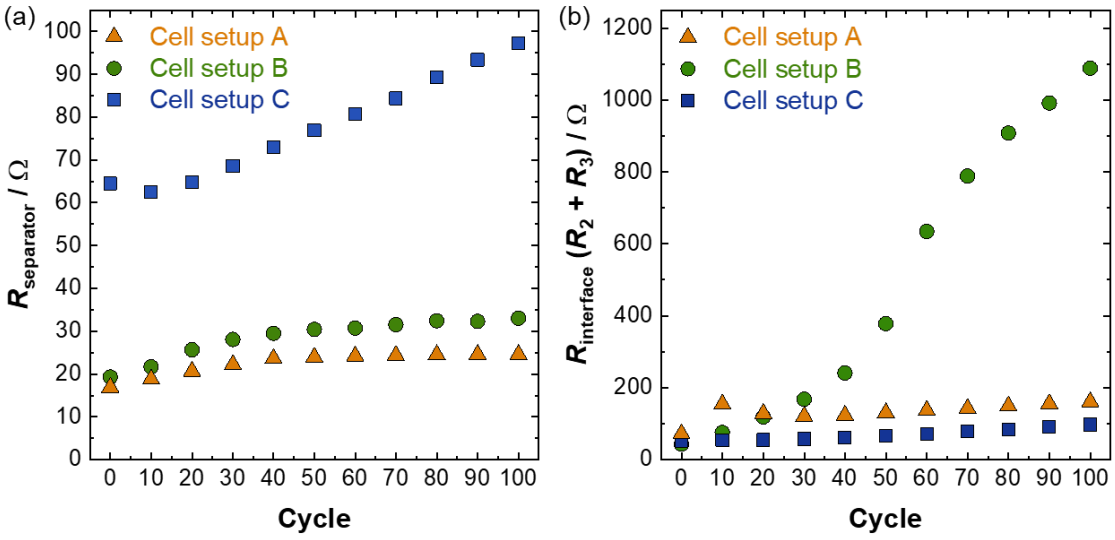

Figure 5: Resistances extracted from the fitted impedance data (a) $R_{separator}$, (b) $R_{interface}$ for cell setup A (orange), B (green) and C (blue) over every tenth cycle from the 1st cycle to the 100th cycle.

2.3 Buried interface analyses

To study the origin of the increased build-up in impedance when halide catholytes are directly in contact with a sulfide separator, cross-sections of cycled cells of cell setup B and C were investigated by FIB-SEM and ToF-SIMS. Figure 6a shows scanning electron micrographs of the polished cross-section of a cycled cell of cell setup B recorded with a back-scattered electron (BSE) and a secondary electron (secondary) detector, respectively. The images show a strong curtaining effect (visible by lines) due to the high roughness of the native cross-sections and related topographic effects during the milling process. Nevertheless, the composite cathode (top) can be well distinguished from the separator (bottom) with both detectors. Due to differences in atomic weights of the compounds, the BSE detector allows, to a certain extent, the differentiation of local changes in the composition. Accordingly, the $LiNi_{0.8}Co_{0.1}Mn_{0.1}O_2$ particles (brighter) can be well distinguished from the Li_3InCl_6 and the Li_6PS_5Cl (darker). Interestingly, an interphase between the composite cathode and the separator is visible, which cannot be seen when using the secondary electron detector. The latter suggests that this feature is not due to topographical effects, but rather has a compositional cause.

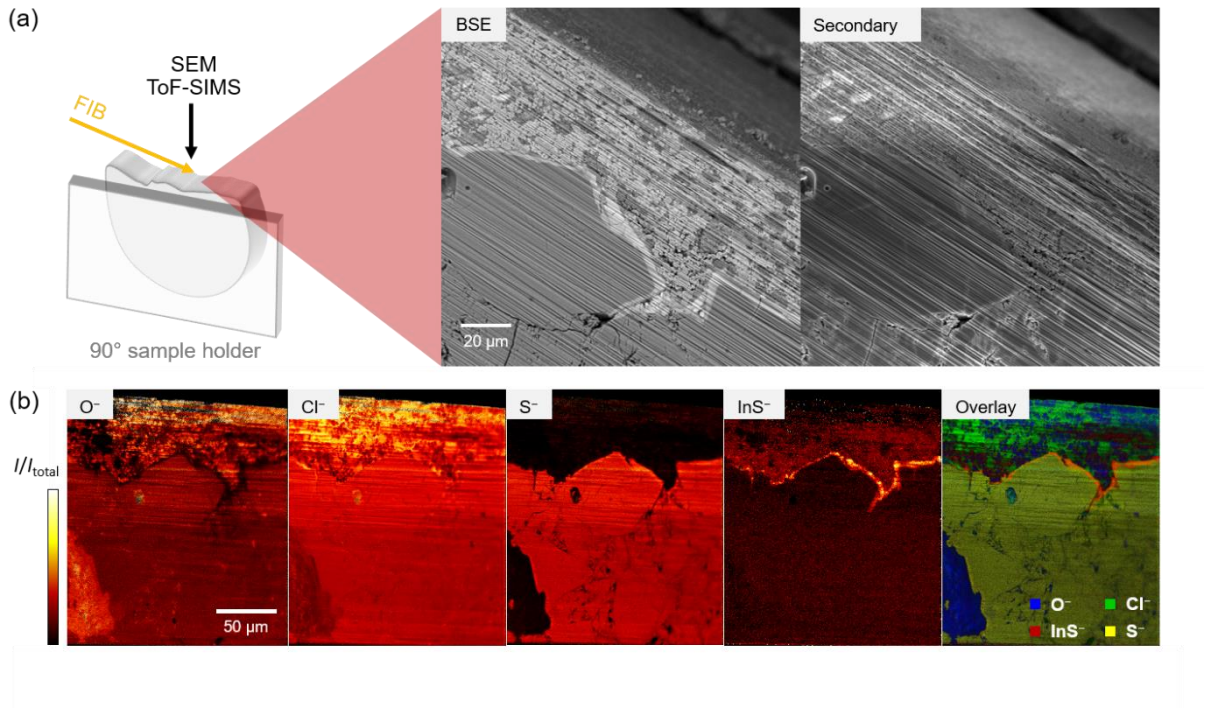

Figure 6: a) Scanning electron micrograph of the polished cross-section of a cycled cell of cell setup B with direct interface between sulfide separator and halide-based cathode composite. A backscattered electron image is shown on the left and a secondary electron image on the right. b) ToF-SIMS imaging of the polished cross-section. Shown are exemplary secondary ion images of negatively charged fragments that allow to distinguish the different components. The specific secondary ion images are normalized in relation to the total ion intensity to reduce topographic effects. For the InS^- fragment, a binning of 16 pixels was used to increase visibility. Both SEM and ToF-SIMS analyses indicate the formation of an interphase between the composite cathode and the separator.

To further study the chemical nature of this interphase, ToF-SIMS imaging was performed on the crater sidewall of the cycled cell. Figure 6b shows that the various compounds can be well distinguished from each other. Accordingly, the $LiNi_{0.8}Co_{0.1}Mn_{0.1}O_2$ particles (represented by O^- fragments) are well separated from Li_3InCl_6 (shows high ionization probability for Cl^- and lack of S^- fragments) and Li_6PS_5Cl (represented by Cl^- and S^- fragments). We found, that the interphase composition is well represented by the InS^- fragment. A possible mass interference with InO_2^- fragments can be ruled out, since no oxygen-related fragments (such as O^-, O_2^- fragments) were detected in these areas. The local peak of the InS^- fragment count indicates the formation of an indium sulfide-like compound in the interfacial region between the composite cathode and the separator. This in turn implies a reaction of Li_3InCl_6 and Li_6PS_5Cl and thus a

thermodynamic instability of both materials in contact to each other, which has been suggested recently.[34,35]

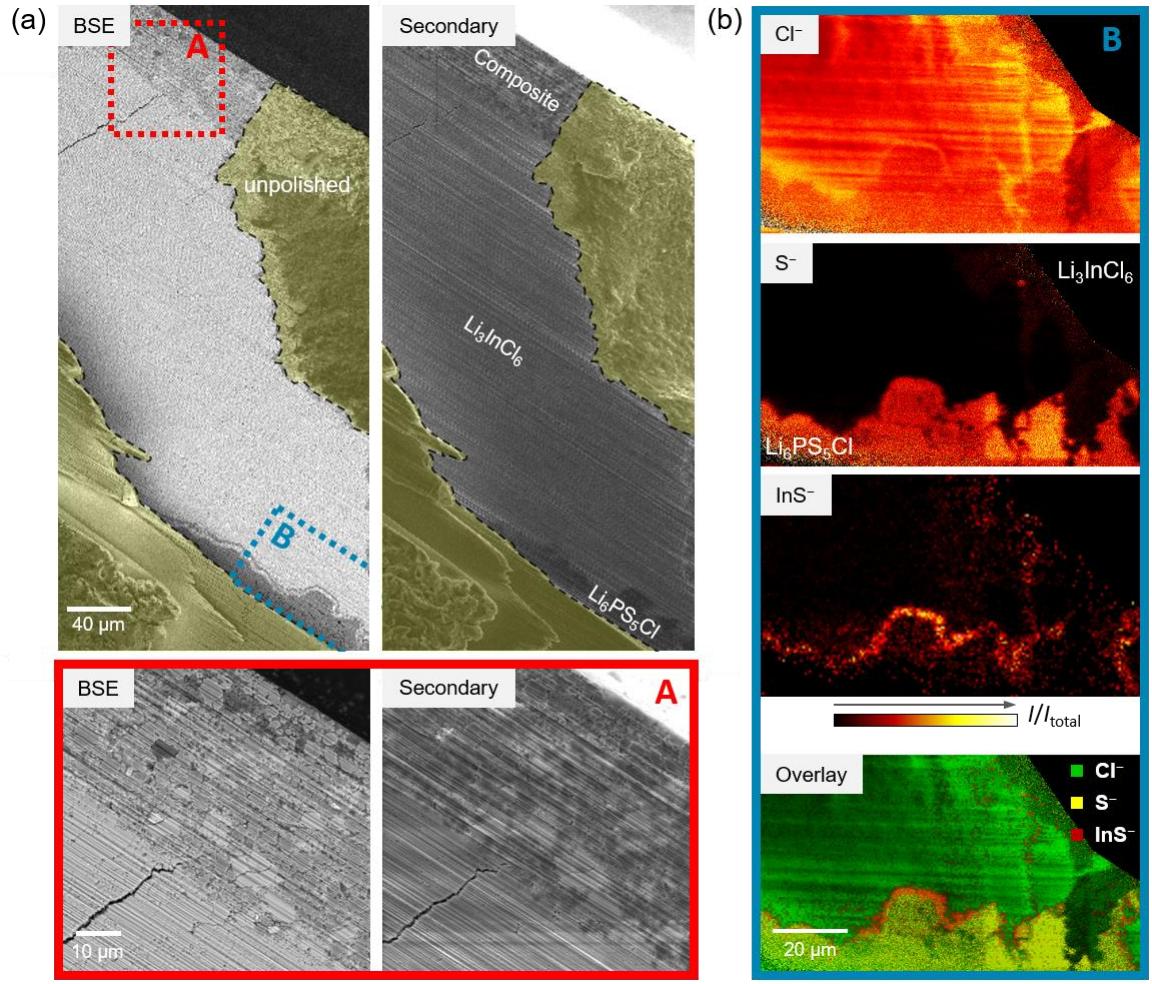

Figure 7: a) Scanning electron micrographs of the polished cross-section of a cycled cell of cell setup C. SE images are shown on the left and BSE images on the right. The composite cathode is shown at the top, the bilayer separator at the bottom. b) ToF-SIMS imaging of the interfacial area between Li_3InCl_6 (top) and Li_6PS_5Cl (bottom). Shown are exemplary secondary ion images of negatively charged fragments that allow to distinguish the different components. The secondary ion images are normalized by the total ion intensity to reduce topographic effects. For the InS^- fragment, a binning of 16 pixels was used to improve contrast. Both SEM and ToF-SIMS analyses indicate the formation of an interphase within the bilayer separator between Li_3InCl_6 and Li_6PS_5Cl.

Analogous measurements were performed for the cycled cell of cell setup C (Figure 7). The additional Li_3InCl_6 layer makes the sample preparation and analysis further challenging, since the interfaces/interphases of interest are buried even deeper and thus the region-of-interest is

much larger. Nevertheless, it was possible to analytically access the composite cathode | separator and the separator | separator (Li_6PS_5Cl | Li_3InCl_6) interfacial regions separately. While no compositional changes were detected at the composite cathode | separator interface, an enrichment of the InS^- fragment was detected at the separator | separator interface (Figure 7 b), similar to the observations above. Compared to cell setup B, the fragment exhibits much less secondary ion intensity. It is difficult to derive (semi-)quantitative conclusions from these measurements, since even small deviations in sample geometry and measurement conditions (e.g., differences in stray electric fields) can significantly influence the results. Nevertheless, it seems that the reaction of Li_3InCl_6 and Li_6PS_5Cl occurs even without the CAM being in close vicinity. As crater milling was not performed under cryo conditions, the highly energetic focused ion beam might be the reason for the apparent reaction between Li_3InCl_6 and Li_6PS_5Cl. To rule this out, in-depth heating experiments of Li_3InCl_6/Li_6PS_5Cl mixtures complemented with XPS and ToF-SIMS analyses were performed. In fact, these control experiments clearly show that the overserved reaction was not induced by the analytical ion beam and a detailed discussion can be found in the Supporting Information.

Overall, the combination of FIB-SEM, XPS and ToF-SIMS analyses confirm a chemical incompatibility of Li_3InCl_6 and Li_6PS_5Cl, leading to the formation of an additional interphase between Li_3InCl_6 and Li_6PS_5Cl. The chemical reaction is predominantly indicated by the formation of indium sulfide-like species in this study.

2.5 Discussion

Overall, the electrochemical testing in this study reveals that a bilayer separator seems necessary for long-term cycling stability of Li_3InCl_6-based composite cathodes when combined with sulfide electrolyte-based separators such as Li_6PS_5Cl. Accordingly, using an additional halide layer to separate the composite cathode from the sulfide separator significantly reduces the impedance evolution upon cell cycling and considerably improves the long-term cycling stability. This implies that the reason for the pronounced cell degradation without the bilayer design lies in the interfacial region between the Li_6PS_5Cl separator and the Li_3InCl_6-based composite cathode. In other words, the presence of the CAM seems to play a strong role. Instrumental analytics confirm that a detrimental chemical reaction of the sulfide and the halide electrolyte at the separator | composite cathode interface causes these issues. Our analytical data indicate a general chemical incompatibility of both solid electrolytes, the reaction of which seems to be further promoted by the close vicinity to the CAM. Accordingly, an interphase is generally formed between Li_6PS_5Cl and Li_3InCl_6, indicated by indium sulfide fragments in the

secondary ion images obtained by ToF-SIMS, and this seems to be more pronounced at the triple phase boundary with the CAM. The following hypotheses for the underlying mechanism can be thought of:

(i) the CAM catalyzes the reaction or causes a larger interfacial contact area that facilitates stronger decomposition,

(ii) the CAM leads to the formation of decomposition products with higher impedances, e.g. $Li_xIn_yS_z$-like compounds are formed as intermediates, which are partially delithiated upon further cycling due to the proximity to the CAM,

(iii) sulfide electrolyte-based decomposition products formed at the interface with the CAM are more reactive with the halide electrolyte than the pristine sulfide electrolyte.

At this stage all these hypotheses are yet highly speculative and require more in-depth analytical studies. Nevertheless, latest theoretical evaluations of the interfacial stability of halide solid electrolytes with charged S_8 and discharged Li_2S cathodes suggest a chemical instability of halides in contact with sulfide species, at least in Li_2S.[52] The chemical reaction of Li_3YCl_6 and Li_3YBr_6 with Li_2S to $LiYS_2$ and LiCl/LiBr seems to be thermodynamically favorable as negative formation enthalpies are found, likely driven by the metal sulfide bond formation. Interestingly these chlorides seem to be chemical stable against S_8, suggesting that the instability stems when sulfide anions are in the vicinity. As Li_2S and polysulfides can be a reaction product of the sulfide electrolyte[32] and Li_6PS_5Cl contains S^{2-} anions, a reaction of Li_3InCl_6 here to In-S species seems reasonable. However, at this stage due to the large phase space at the triple phase boundary of the CAM, Li_3InCl_6 and Li_6PS_5Cl a direction reaction pathway remains speculative. Nevertheless, these findings support the reaction products of the two electrolytes Li_6PS_5Cl and Li_3InCl_6 that were found here, with InS^- fragments stemming potentially from In_2S_3 or $LiInS_2$ and concurrent LiCl decomposition products.

While the halide–sulfide combination does not seem ideal, possible protection of the metal anode *via* polymers or oxide separators may be a future option. In addition, a separation of the sulfide and halide interphase with a thin Li_3PO_4 coating by atomic layer deposition is possible and can increase the cycle stability.[35] As recent work has shown that the chemical stability of halides against CAM centers around the metal ion in Li-M-Cl, the chemical stability against sulfides may also be a function of the halide solid electrolyte composition, indicating the need to search for more stable combinations at the triple phase boundary.[33] This is further substantiated as the Li_3InCl_6-based cell, with Li_3InCl_6 in the composite and double separator

layer, showed growth in the $R_{separator}$ resistance as well, whereas the other two tested single-layer separators did not. Interestingly, $Li_{2.5}Y_{0.5}Zr_{0.5}Cl_6$, one of the halide electrolytes compositions that were found stable against $LiNi_{1/3}Co_{1/3}Mn_{1/3}O_2$ showed no good stability against the oxygen release of $LiNi_{0.85}Co_{0.1}Mn_{0.05}O_2$. In contrast, Li_3InCl_6 has a lower stability against electrochemical oxidation compared to $Li_2In_{1/3}Sc_{1/3}Cl_4$.[33] Overall, these results highlight that the search for new electrolytes should be inspired by the chemical compatibility of the compounds to the desired CAM and other potential components and taking possible reactions into account.

3. Conclusions

In this study, we analyzed the role of a bilayer separator for halide-based composite cathodes when combined with sulfide-based separators, using Li_3InCl_6 and Li_6PS_5Cl as an example. We have shown that an additional halide separatorlayer separating the composite cathode from the sulfide-based separator is crucial for the cycling stability. Accordingly, the capacity retention was significantly increased and the impedance evolution upon cycling was suppressed coming in the performance range of pure sulfide based cells, explaining why the bilayer design is often chosen in the literature. Using FIB-SEM and ToF-SIMS analyses, we were able to visualize the chemical incompatibility of the two electrolytes Li_3InCl_6 and Li_6PS_5Cl. The accompanied interphase formation, indicated by indium sulfide-based degradation products, is of a general nature, but seems to be further promoted at the triple phase boundary with contact to the CAM. This leads to a strong rise in the impedance and a rapid capacity fading upon cell cycling, when only one separator layer is used. However, one may suspect that the general chemical incompatibility of both electrolytes may be a problem for long-term stability, even if the bilayer design is used.

Overall, the results of this study emphasize the importance of considering the chemical stability of all cell components relative to each other. Research currently often focuses on the stability or chemical compatibility of compounds towards the electrodes, motivating bi- or even multilayer designs for solid-state batteries neglecting the increasing number of interfaces and possible degradation spots, i.e. evolving interphases. However, reactivity beyond the electrodes is often overlooked so far, which can easily lead to severe capacity fading and poor long-term cycling stability, as shown in this study. Therefore, besides high electrochemical stability of the solid electrolyte towards high potential active materials, the chemical stability within the different battery components must be taken more into account and novel protection concepts or more stable materials need to be developed.

Supporting Information

Experimental information, refinement and impedance fit of the electrolytes Li_3InCl_6 and Li_6PS_5Cl, discharge capacities, Coulomb efficiencies, impedance spectra for all cell setups over cycling, impedance fit parameter for frequency range, α-values, capacitances and resistances, XPS and ToF-SIMS analysis of untreated and heated Li_3InCl_6:Li_6PS_5Cl mixture, calculation of wt% to vol% for the cathode composites, voltage / stability windows of the cell components.

Acknowledgements

The authors acknowledge financial support within the cluster of competence FESTBATT funded by Bundesministerium für Bildung und Forschung (BMBF; projects 03XP0430A, 03XP0430F). The authors acknowledge Björn Wankmiller for measuring ^{7}Li and ^{31}P MAS NMR (not shown). MH and BW are members of the International Graduate School for Battery Chemistry, Characterization, Analysis, Recycling and Application (BACCARA), which is funded by the Ministry for Culture and Science of North Rhine-Westphalia, Germany. SO acknowledge financial support from JSPS KAKENHI grant number JP 21K14720.

References

[1] J. Janek, W. G. Zeier, *Nat. Energy* **2016**, *1*, 16141.

[2] S. Randau, D. A. Weber, O. Kötz, R. Koerver, P. Braun, A. Weber, E. Ivers-Tiffée, T. Adermann, J. Kulisch, W. G. Zeier, F. H. Richter, J. Janek, *Nat. Energy* **2020**, *5*, 259–270.

[3] A. Manthiram, X. Yu, S. Wang, *Nat. Rev. Mater.* **2017**, *2*, 16103.

[4] Y. Kato, S. Hori, T. Saito, K. Suzuki, M. Hirayama, A. Mitsui, M. Yonemura, H. Iba, R. Kanno, *Nat. Energy* **2016**, *1*, 16030.

[5] S. Ohno, A. Banik, G. F. Dewald, M. A. Kraft, T. Krauskopf, N. Minafra, P. Till, M. Weiss, W. G. Zeier, *Prog. Energy* **2020**, *2*, 022001.

[6] Y. S. Jung, D. Y. Oh, Y. J. Nam, K. H. Park, *Isr. J. Chem.* **2015**, *55*, 472–485.

[7] A. Gautam, M. Ghidiu, E. Suard, M. A. Kraft, W. G. Zeier, *ACS Appl. Energy Mater.* **2021**, *4*, 7309–7315.

[8] A. Gautam, M. Sadowski, M. Ghidiu, N. Minafra, A. Senyshyn, K. Albe, W. G. Zeier, *Adv. Energy Mater.* **2021**, *11*, 2003369.

[9] N. Minafra, M. A. Kraft, T. Bernges, C. Li, R. Schlem, B. J. Morgan, W. G. Zeier, *Inorg. Chem.* **2020**, *59*, 11009–11019.

[10] K. Homma, M. Yonemura, T. Kobayashi, M. Nagao, M. Hirayama, R. Kanno, *Solid State Ionics* **2011**, *182*, 53–58.

[11] Z. Liu, W. Fu, E. A. Payzant, X. Yu, Z. Wu, N. J. Dudney, J. Kiggans, K. Hong, A. J. Rondinone, C. Liang, *J. Am. Chem. Soc.* **2013**, *135*, 975–978.

[12] S. P. Culver, A. G. Squires, N. Minafra, C. W. F. Armstrong, T. Krauskopf, F. Böcher, C. Li, B. J. Morgan, W. G. Zeier, *J. Am. Chem. Soc.* **2020**, *142*, 21210–21219.

[13] T. Krauskopf, S. P. Culver, W. G. Zeier, *Chem. Mater.* **2018**, *30*, 1791–1798.

[14] W. Zhang, D. A. Weber, H. Weigand, T. Arlt, I. Manke, D. Schröder, R. Koerver, T. Leichtweiss, P. Hartmann, W. G. Zeier, J. Janek, *ACS Appl. Mater. Interfaces* **2017**, *9*, 17835–17845.

[15] J. Ruhl, L. M. Riegger, M. Ghidiu, W. G. Zeier, *Adv. Energy Sustain. Res.* **2021**, *2*, 2000077.

[16] R. Koerver, I. Aygün, T. Leichtweiß, C. Dietrich, W. Zhang, J. O. Binder, P. Hartmann, W. G. Zeier, J. Janek, *Chem. Mater.* **2017**, *29*, 5574–5582.

[17] A. Sakuda, A. Hayashi, M. Tatsumisago, *Sci. Rep.* **2013**, *3*, 2261.

[18] L. L. Baranowski, C. M. Heveran, V. L. Ferguson, C. R. Stoldt, *ACS Appl. Mater. Interfaces* **2016**, *8*, 29573–29579.

[19] F. Walther, R. Koerver, T. Fuchs, S. Ohno, J. Sann, M. Rohnke, W. G. Zeier, J. Janek, *Chem. Mater.* **2019**, *31*, 3745–3755.

[20] T. Asano, A. Sakai, S. Ouchi, M. Sakaida, A. Miyazaki, S. Hasegawa, *Adv. Mater.* **2018**, *30*, 1803075.

[21] X. Li, J. Liang, X. Yang, K. R. Adair, C. Wang, F. Zhao, X. Sun, *Energy Environ. Sci.* **2020**, *13*, 1429–1461.

[22] B. Helm, R. Schlem, B. Wankmiller, A. Banik, A. Gautam, J. Ruhl, C. Li, M. R. Hansen, W. G. Zeier, *Chem. Mater.* **2021**, *33*, 4773–4782.

[23] K.-H. Park, K. Kaup, A. Assoud, Q. Zhang, X. Wu, L. F. Nazar, *ACS Energy Lett.* **2020**, *5*, 533–539.

[24] R. Schlem, T. Bernges, C. Li, M. A. Kraft, N. Minafra, W. G. Zeier, *ACS Appl. Energy Mater.* **2020**, *3*, 3684–3691.

[25] X. Li, J. Liang, N. Chen, J. Luo, K. R. Adair, C. Wang, M. N. Banis, T. Sham, L. Zhang, S. Zhao, S. Lu, H. Huang, R. Li, X. Sun, *Angew. Chemie Int. Ed.* **2019**, *58*, 16427–16432.

[26] X. Li, J. Liang, J. Luo, M. Norouzi Banis, C. Wang, W. Li, S. Deng, C. Yu, F. Zhao, Y. Hu, T.-K. Sham, L. Zhang, S. Zhao, S. Lu, H. Huang, R. Li, K. R. Adair, X. Sun, *Energy Environ. Sci.* **2019**, *12*, 2665–2671.

[27] R. Schlem, A. Banik, S. Ohno, E. Suard, W. G. Zeier, *Chem. Mater.* **2021**, *33*, 327–337.

[28] R. Schlem, S. Muy, N. Prinz, A. Banik, Y. Shao-Horn, M. Zobel, W. G. Zeier, *Adv. Energy Mater.* **2020**, *10*, 1903719.

[29] L. Zhou, C. Y. Kwok, A. Shyamsunder, Q. Zhang, X. Wu, L. F. Nazar, *Energy Environ. Sci.* **2020**, *13*, 2056–2063.

[30] S. Wang, Q. Bai, A. M. Nolan, Y. Liu, S. Gong, Q. Sun, Y. Mo, *Angew. Chemie* **2019**, *131*, 8123–8127.

[31] D. Park, H. Park, Y. Lee, S.-O. Kim, H.-G. Jung, K. Y. Chung, J. H. Shim, S. Yu, *ACS Appl. Mater. Interfaces* **2020**, *12*, 34806–34814.

[32] L. Zhou, N. Minafra, W. G. Zeier, L. F. Nazar, *Acc. Chem. Res.* **2021**, *54*, 2717–2728.

[33] I. Kochetkov, T.-T. Zuo, R. Ruess, B. Singh, L. Zhou, K. Kaup, J. Janek, L. Nazar, *Energy Environ. Sci.* **2022**, *15*, 3933–3944.

[34] T. Koç, F. Marchini, G. Rousse, R. Dugas, J.-M. Tarascon, *ACS Appl. Energy Mater.* **2021**, *4*, 13575–13585.

[35] T. Koç, M. Hallot, E. Quemin, B. Hennequart, R. Dugas, A. M. Abakumov, C. Lethien, J.-M. Tarascon, *ACS Energy Lett.* **2022**, *7*, 2979–2987.

[36] L. M. Riegger, R. Schlem, J. Sann, W. G. Zeier, J. Janek, *Angew. Chemie Int. Ed.* **2021**, *60*, 6718–6723.

[37] C. Wang, J. Liang, J. Luo, J. Liu, X. Li, F. Zhao, R. Li, H. Huang, S. Zhao, L. Zhang, J. Wang, X. Sun, *Sci. Adv.* **2021**, *7*, DOI 10.1126/sciadv.abh1896.

[38] L. Zhou, T.-T. Zuo, C. Y. Kwok, S. Y. Kim, A. Assoud, Q. Zhang, J. Janek, L. F. Nazar, *Nat. Energy* **2022**, *7*, 83–93.

[39] X. Shi, Z. Zeng, M. Sun, B. Huang, H. Zhang, W. Luo, Y. Huang, Y. Du, C. Yan, *Nano Lett.* **2021**, *21*, 9325–9331.

[40] M. A. Kraft, S. P. Culver, M. Calderon, F. Böcher, T. Krauskopf, A. Senyshyn, C. Dietrich, A. Zevalkink, J. Janek, W. G. Zeier, *J. Am. Chem. Soc.* **2017**, *139*, 10909–10918.

[41] P. Minnmann, L. Quillman, S. Burkhardt, F. H. Richter, J. Janek, *J. Electrochem. Soc.* **2021**, *168*, 040537.

[42] L. de Biasi, B. Schwarz, T. Brezesinski, P. Hartmann, J. Janek, H. Ehrenberg, *Adv. Mater.* **2019**, *31*, 1900985.

[43] T. Li, X.-Z. Yuan, L. Zhang, D. Song, K. Shi, C. Bock, *Electrochem. Energy Rev.* **2020**, *3*, 43–80.

[44] R. Koerver, W. Zhang, L. de Biasi, S. Schweidler, A. O. Kondrakov, S. Kolling, T. Brezesinski, P. Hartmann, W. G. Zeier, J. Janek, *Energy Environ. Sci.* **2018**, *11*, 2142–2158.

[45] D. H. S. Tan, E. A. Wu, H. Nguyen, Z. Chen, M. A. T. Marple, J.-M. Doux, X. Wang, H. Yang, A. Banerjee, Y. S. Meng, *ACS Energy Lett.* **2019**, *4*, 2418–2427.

[46] S. Ohno, C. Rosenbach, G. F. Dewald, J. Janek, W. G. Zeier, *Adv. Funct. Mater.* **2021**, *31*, 2010620.

[47] N. Kaiser, S. Spannenberger, M. Schmitt, M. Cronau, Y. Kato, B. Roling, *J. Power Sources* **2018**, *396*, 175–181.

[48] V. Miß, A. Ramanayagam, B. Roling, *ACS Appl. Mater. Interfaces* **2022**, *14*, 38246–

38254.

[49] R. Koerver, F. Walther, I. Aygün, J. Sann, C. Dietrich, W. G. Zeier, J. Janek, *J. Mater. Chem. A* **2017**, *5*, 22750–22760.

[50] J. K. Eckhardt, T. Fuchs, S. Burkhardt, P. J. Klar, J. Janek, C. Heiliger, *ACS Appl. Mater. Interfaces* **2022**, *14*, 42757–42769.

[51] G. H. Chun, J. H. Shim, S. Yu, *ACS Appl. Mater. Interfaces* **2022**, *14*, 1241–1248.

[52] M. L. Holekevi Chandrappa, J. Qi, C. Chen, S. Banerjee, S. P. Ong, *J. Am. Chem. Soc.* **2022**, *144*, 18009–18022.